Acta Crystallographica Section D
Biological Crystallography
ISSN 0907-4449

Spatial dependence and mitigation of radiation damage by a line-focus mini-beam

Y. Zou Finfrock,[a] Edward A. Stern,[a]* Yizhak Yacoby,[b] R. W. Alkire,[c] Kenneth Evans-Lutterodt,[d] Aaron Stein,[d] Abdel F. Isakovic,[d]‡ Joshua J. Kas[a] and Andrzej Joachimiak[e]

[a]Physics Department, University of Washington, Seattle, Washington 98195-1560, USA, [b]Racah Institute of Physics, Hebrew University, Jerusalem, Israel, [c]Structural Biology Center, Argonne National Laboratory, Argonne, IL 60439, USA, [d]National Synchrotron Light Source, Brookhaven National Laboratory, Upton, NY 11973, USA, and [e]Center for Mechanistic Biology and Biotechnology, Argonne National Laboratory, Argonne, IL 60439, USA

‡ Current address: Khalifa University of Science, Technology and Research (KUSTAR), PO Box 127788, Abu Dhabi, United Arab Emirates.

Correspondence e-mail: stern@phys.washington.edu

Received 20 April 2010
Accepted 14 September 2010

Recently, strategies to reduce primary radiation damage have been proposed which depend on focusing X-rays to dimensions smaller than the penetration depth of excited photoelectrons. For a line focus as used here the penetration depth is the maximum distance from the irradiated region along the X-ray polarization direction that the photoelectrons penetrate. Reported here are measurements of the penetration depth and distribution of photoelectron damage excited by 18.6 keV photons in a lysozyme crystal. The experimental results showed that the penetration depth of ∼17.35 keV photoelectrons is 1.5 ± 0.2 μm, which is well below previous theoretical estimates of 2.8 μm. Such a small penetration depth raises challenging technical issues in mitigating damage by line-focus mini-beams. The optimum requirements to reduce damage in large crystals by a factor of 2.0–2.5 are Gaussian line-focus mini-beams with a root-mean-square width of 0.2 μm and a distance between lines of 2.0 μm. The use of higher energy X-rays (>26 keV) would help to alleviate some of these requirements by more than doubling the penetration depth. It was found that the X-ray dose has a significant contribution from the crystal's solvent, which initially contained 9.0%(*w*/*v*) NaCl. The 15.8 keV photoelectrons of the Cl atoms and their accompanying 2.8 keV local dose from the decay of the resulting excited atoms more than doubles the dose deposited in the X-ray-irradiated region because of the much greater cross-section and higher energy of the excited atom, degrading the mitigation of radiation damage from 2.5 to 2.0. Eliminating heavier atoms from the solvent and data collection far from heavy-atom absorption edges will significantly improve the mitigation of damage by line-focus mini-beams.

1. Introduction

Radiation damage is an important issue in macromolecular crystallography, especially using synchrotron radiation, and various aspects of this problem have been systematically investigated by numerous researchers. There have been significant advances in the understanding of radiation damage over the past few years (Borek *et al.*, 2007, 2010; Petrova *et al.*, 2009, 2010; Takeda *et al.*, 2010; Nowak *et al.*, 2009; Holton, 2009; Paithankar *et al.*, 2009; Garman & Nave, 2009; Cowan & Nave, 2008; Southworth-Davies *et al.*, 2007; Meents *et al.*, 2007; Garman & McSweeney, 2007; Kmetko *et al.*, 2006; Ravelli & Garman, 2006). Radiation damage in macromolecular crystallography includes the primary damage caused by electrons directly excited in biological matter and solvent. At the X-ray energies used in macromolecular crystallography, less than 15% of X-rays result in productive diffraction events; the remaining X-rays impart energy to biological crystals that

results in damage (Sliz *et al.*, 2003; Gonzalez & Nave, 1994). Therefore, much effort has been applied to understanding and reducing damage. Secondary damage is induced by primary damage, which creates a cascade of highly reactive radiolytic species that propagate through the crystal, react with the macromolecules and cause further damage. Secondary damage has been significantly reduced by collecting data from cryopreserved crystals (Meents *et al.*, 2007, 2010; Petrova *et al.*, 2010; Holton, 2009; Garman & Nave, 2009; Chinte *et al.*, 2007; Garman & McSweeney, 2007; Kmetko *et al.*, 2006; Ravelli & Garman, 2006).

However, primary damage is still a large problem even with cryoprotected crystals. Recently, techniques to minimize primary radiation damage have been suggested. They all use the principle of separating the irradiated region from the damaging photoelectrons (PEs) as much as is feasible (Nave & Hill, 2005; Cowan & Nave, 2008; Stern *et al.*, 2009). In standard crystallography, it is conjectured that PEs typically deposit damage several micrometres away from their excited atoms, which are the main cause of the primary damage. This has led to the suggestion of using X-ray beams focused to dimensions that are small compared with the PE penetration depth. It has been reported that a mini-beam significantly improved the signal-to-noise ratios for data collected from small crystals (Sanishvili *et al.*, 2008) because it reduced the background by concentrating the radiation on the crystal. A recent paper showed that a 1 µm size point-focus beam could collect a complete data set for a known protein structure (Moukhametzianov *et al.*, 2008). However, using a small beam to achieve the same diffraction signal as a larger beam requires more exposure in the irradiated region and to alleviate this for the point focus the authors spread the beam around a greater crystal volume by moving the focus somewhat off the crystal rotation axis.

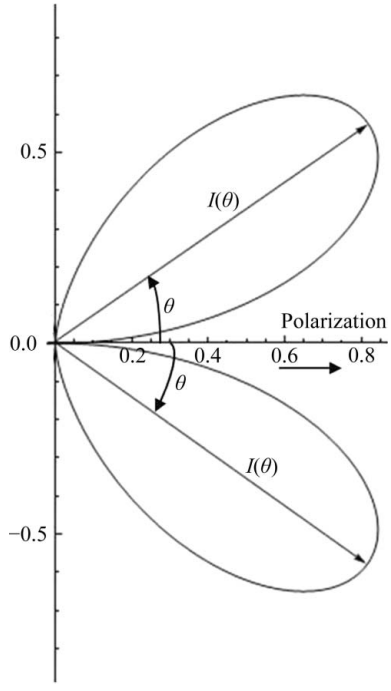

Figure 1
The intensity of PE emission as a function of θ for horizontally polarized X-rays from a synchrotron source. Shown is a slice in a vertical plane of the doughnut-like distribution of the emission, which has rotation symmetry about the polarization direction and mirror symmetry about the plane normal to the polarization (the latter is not shown). The PE flux from excited atoms is emitted outwards along the polarization direction.

The implementation of these ideas depends strongly on the PE penetration depth and the damage created in and outside the irradiated region. In this paper, we report measurements of the PE penetration depth for 18.6 keV X-rays and the spatial dependence of damage in and outside the irradiated region.

The primary damage has two main mechanisms, both of which are related to the photoelectric effect. The absorption of an X-ray photon transfers its energy to a bonded electron in the atom, emitting it as a PE. Part of the energy of the X-ray photon is transferred to the atom to overcome the binding energy of the electron and the remainder of its energy is transferred to the PE. The excited atom deposits its energy into its local neighborhood by emission of low-energy Auger electrons, while the PE deposits its excess energy over its path of typically a few micrometres, causing local and nonlocal damage, respectively.

In Stern *et al.* (2009), it is shown that for the X-ray energies utilized in macromolecular crystallography the PE emission distribution varies closely as $\cos^2\theta$ relatively independently of X-ray energy and atomic number, where θ is the angle between the beam-polarization vector and the initial PE velocity vector. However, this does not mean that the emission peaks at $\theta = 0$ because this distribution is per solid angle (equal to $\sin\theta\,d\theta\,d\varphi$). To find the dependence on θ requires integrating over $d\varphi$, leading to a distribution proportional to $\cos^2\theta\sin\theta$ as shown in Fig. 1. The average angle of PE emission is 38.2° and the largest intensity is at 35.3°. Since the distribution has rotational symmetry about the polarization (x direction), the component of the flux perpendicular to the x direction averages to zero and the total PE flux flows outwards from its source along the horizontal X-ray polarization. Therefore, a vertical line-focus mini-beam will most efficiently direct PE damage outside of the irradiated region. The initial emission direction of a PE always has a component perpendicular to x. However, this component of the total flux is cancelled by another PE emitted at a φ 180° away. Thus, on average only the x components of both the initial flux and the penetration distance survive and are 2/3 of their magnitudes along the initial PE direction (Stern *et al.*, 2009). The line focus will also significantly reduce the damage for a given diffraction signal compared with a point focus because of the larger irradiated region. This paper reports the results of measurements using a line-focus mini-beam to determine the PE penetration depth in a protein crystal. This result is important in quantifying the strategy to reduce primary radiation damage in macromolecular crystallography (Stern *et al.*, 2009).

2. Experimental details and measurements

The SBC 19-ID beamline at the Advanced Photon Source has mechanical bearings on its ω drive, which moves several

micrometres horizontally during the large angular rotation for data collection, broadening the line-focus irradiated region. In order to reduce this excessive horizontal motion to within the target accuracy of ∼0.1 µm, only a 3° variation was used in our measurements. As discussed in §4, this target was successfully attained.

The line-focus lens was made in a single-crystal silicon wafer by using microfabrication techniques (Evans-Lutterodt *et al.*, 2003). The lens is about 5 mm long with an elliptical profile; the entrance width is about 20 µm and etched down to L = 25 µm depth. For the lens alignment, six degrees of freedom are utilized. The *x*-, *y*- and *z*-axis linear motions bring the lens to the X-ray beam and three rotation axes are used to orient the lens to maximize the beam intensity by assuring that the X-ray beam goes through the whole lens.

The refractive lens is designed to produce a line-focus mini-beam of 1–2 µm wide by 25 µm long with a 60 mm focal length at 19 keV X-ray energy. The beam profile was characterized with a 70 µm wide and 30 nm thick Cr layer knife-edge by scanning its 30 nm thick layer through the focus with a linear drive capable of 7.7 nm per step resolution. An NaI (Tl) scintillation detector was used to measure the Cr fluorescence signal. The beam profile and its fits are shown in Fig. 2. The variation of the profile near the focus was also measured and found to be quite constant for a distance of 5 mm on either side of the focus. Because the practical upper energy limit for the 19-ID monochromator is 18.6 keV, which is 0.4 keV below the lens design value, the resulting focal length is slightly shorter than 60 mm. The beam profile and fits in Fig. 2 include a sharp Gaussian component and a broad Lorentzian component comprising the wide tails. It was suspected that the tails were somewhat enhanced and they were corrected as per the deconvolution fit discussed in §4.

The experiments were performed on a tetragonal lysozyme crystal (space group $P4_32_12$, unit-cell parameters $a = b = 78.87$, $c = 36.84$ Å (Hanson *et al.*, 2002; PDB code 1lz8) at 18.6 keV with a single lens at 2.86×10^8 photons s^{-1} photon flux. The crystal incorporated 41% solvent, which initially contained 9.0%(*w*/*v*) NaCl in the mother liquor. Calculations were made to estimate the change in the Na and Cl atoms incorporated in the crystal and were further refined by comparison with the $\rho = 1.23$ g cm^{-1} specific weight of the lysozyme crystal (Leung *et al.*, 1999).

Probing diffraction data were collected with 20 s per image exposure time with 0.5° oscillation over a 3° angle range. Diffraction patterns were recorded on an ADSC Quantum 315r CCD detector while the sample crystal was kept in a 100 K cryostream flow (Alkire *et al.*, 2008). The sample-to-detector distance was 250 mm. The crystal diffracted well beyond 1.5 Å resolution with a high signal-to-background ratio. There were two processes in the experiment. Firstly, a data set was collected as a probe of the fresh crystal. The crystal was then damaged with an extended exposure time of 60 s per image and the crystal was probed again. The damage/probe sequence was repeated eight times for a total exposure of T_d = 3960 s. Afterwards, the sample was moved by a pico-motor relative to the lens with 1.0 ± 0.08 µm steps to probe the spatial dependence of radiation damage outside of the initial highly damaged region. The probing time was T_O = 120 s.

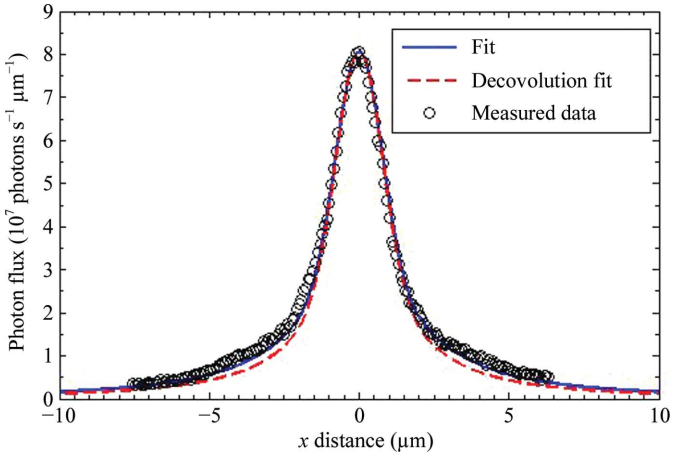

Figure 2
The measured beam profile (open dots) at 18.6 keV, the fit (solid line) and the deconvolution fit (dashed line). The deconvolution fit consists of the sum of a Gaussian with 1.05 µm root-mean-square width and a Lorentzian tail.

3. Analysis and results

The damage was determined by an analysis of the experimental data using the *HKL* software package (Minor *et al.*, 2006) to determine the overall relative B factor as a measure of the damage. The relative B factor was determined by dividing the diffraction signal into a series of resolution shells and was then scaled using the *SCALEPACK* program. The resulting relative B factor is proportional to the change in the isotropic mean-squared atomic displacements $\Delta(u^2) = B/8\pi^2$. The $\Delta(u^2)$ decrease the intensity of the Bragg spots by the Debye–Waller factor of $\exp(-B/4r_j^2)$ in the r_j resolution shell.

Fig. 3 shows the resulting B factor as a function of exposure at the initial highly damaged site. The first data point is damaged by its exposure on the fresh crystal. Setting $B = 0$ for

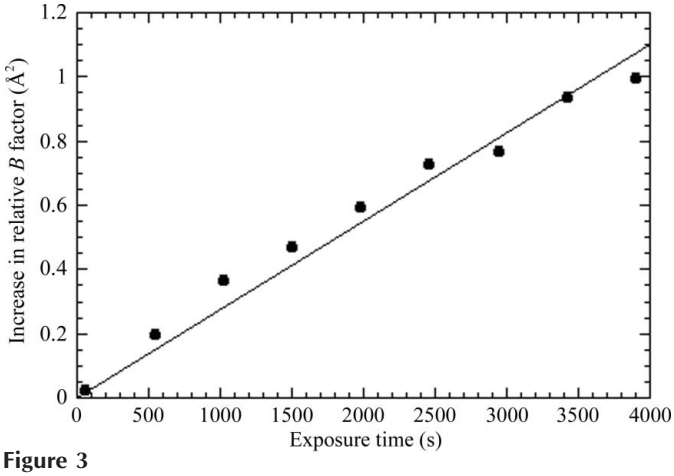

Figure 3
Relative B factor as a function of exposure time. The straight line is fitted to the data.

the fresh crystal, the first data point is found to be at $B = 0.025$ Å^2 by extrapolating to zero exposure. Note that the B factors are all at or below a value of 1. The maximum value of the $B/4r_j^2$ argument of the Debye–Waller factor is 0.094 at the highest usable resolution shell centered at 1.63 Å. This low value allows the approximation of the Debye–Waller factor by its linear first-order expansion in the argument of $1 - B/4r_j^2$.

As will be pointed out in §5, the linear behavior of the Debye–Waller factor produces a correct averaging of B throughout the focus profile of Fig. 2, where the intensity is varying greatly.

In Fig. 4 the solid circles show the measured B factor as a function of probing distance from the center of the initially highly damaged site. The deconvolution of these data is presented in the next section. Again, the linear approximation for the Debye–Waller factor is valid, producing a correct averaging of B throughout the focus profile.

4. Deconvolution

The experimentally observed damage presented in Fig. 4 is a result of the specific beam shape and measurement procedure we have used. In this section, we assume that the damage at any point in the sample is proportional to the energy per unit mass (dose) deposited by the X-ray-excited electrons at the point. As mentioned above, in the PE effect for typical protein atoms two mechanisms dominate in completely converting an absorbed X-ray photon into excited electrons. One is the creation of a PE which distributes its energy over its path and the other is the decay of the excited atom by emitting low-energy Auger electrons locally. The photons also excite low-energy Compton electrons by inelastic scattering, which contribute to the local dose. Low-energy Auger and Compton electrons represent a small fraction of deposited energy, do not travel far and are captured within the irradiated region. The PE dose is by far the greatest, so that it is important to determine its penetration depth for the design of the X-ray focus to separate its dose from the irradiated region. Unfortunately, the focus provided by the lens was not small compared with the penetration depth of the PE, so it was necessary to deconvolute the data in order to obtain an accurate measure of this penetration depth.

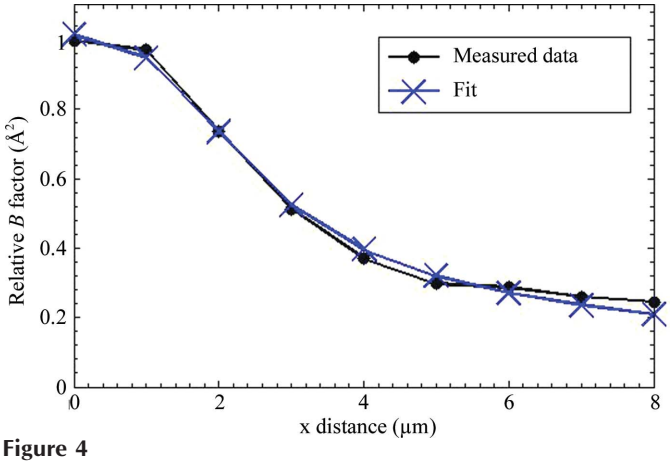

Figure 4
Measured experimental data with a deconvolution fit of the spatial dependence of radiation damage as function of x distance.

Table 1
Symbols, units and values.

Symbol	Value
E_{PH} (keV)	18.6
η_L	0.075
η_{PE}	0.93
T_D (s)	3960
T_O (s)	120
μ (μm^{-1})	0.945×10^{-4}
ρ (g cm^{-3})	1.23
I_G (photons s^{-1} μm^{-1})	5.1×10^7
σ_G^2 (μm^2)	1.1
I_{LO} (photons s^{-1} μm^{-1})	3.1×10^7
σ_L^2 (μm^2)	5.8
σ_{LO}^2 (μm^2)	4.2
L (μm)	25
a (keV μm^{-1})	2.32
β	4.2
α (μm^{-1})	2.8
d (μm)	1.5
γ (Å^2 MGy^{-1})	0.75
σ_{opt} (μm)	0.20
d_{opt} (μm)	2.0
Optimal mitigation	2.0

To a good approximation, the line-focused X-ray beam intensity varies in only the x direction along the X-ray polarization perpendicular to the line of focus. $I(x)$ is defined as the X-ray energy absorbed per unit mass at a distance x from the center of the focal line. Note that this energy is not necessarily deposited at x because of the emission of PEs. The change in damage at x induced by a unit energy per unit mass absorbed in the region between x' and $x' + dx'$ is $\overline{B}(x - x')\,dx'$. Therefore, the damage at a point x is given by

$$B(x) = \int_{-\infty}^{\infty} \overline{B}(x - x')I(x')\,dx'. \quad (1)$$

$\overline{B}$ can be divided into two components:

$$\overline{B}(x - x') = \overline{B}_L\delta(x - x') + \overline{B}_{PE}(x - x'). \quad (2)$$

The first arises from the emission of Auger and Compton electrons causing damage locally of amount $\overline{B}_L I(x)$, while the second arises from the PE causing damage in an extended region.

When measuring the damage the same line-focused beam is used, so the observed damage B_O is

$$B_O(x) \simeq \int_{-\infty}^{\infty} B(x')I_P(x - x')\,dx' \Big/ \int_{-\infty}^{\infty} I_P(x')\,dx'. \quad (3)$$

Here, $I_P(x - x')$ is the much weaker probing intensity with the same spatial dependence but centered at x. Notice that each time the damage is probed additional damage is introduced from $I_P(x - x')$. This extra damage is accounted for in the deconvolution calculation.

As discussed previously, the experimental beam shape was fitted using a combination of a Gaussian and a Lorentzian as shown in Fig. 2,

$$I(x) = I_{\rm G}\exp\left(-\frac{x^2}{\sigma_{\rm G}^2}\right) + \frac{I_{\rm LO}\sigma_{\rm L}^2}{x^2+\sigma_{\rm L}^2}. \quad (4)$$

The values of these and all other parameters are presented in Table 1.

It was suspected that the large tails observed in Fig. 2 may partially arise from contributions above and below the focal line. Therefore, the Lorentzian was allowed to change in the following way:

$$I(x) = I_{\rm G}\exp\left(-\frac{x^2}{\sigma_{\rm G}^2}\right) + \frac{I_{\rm LO}\sigma_{\rm LO}^2}{x^2+\sigma_{\rm LO}^2}. \quad (5)$$

Thus, $\sigma_{\rm LO}^2$ is the first parameter in fitting the experimentally measured and calculated damage. Note that varying $\sigma_{\rm LO}^2$ changes the tails of the distribution, leaving the value at the peak unchanged.

The stopping power, which is defined as the energy deposited by a PE per micrometre, varies with the distance traveled from its source. Initially, when its energy is large, the stopping power and scattering are small. The PE stopping power and scattering increase as it loses energy. These two factors combine to increase the PE energy deposition per unit length along the polarization direction. This energy deposition per unit length increases to a maximum near a PE energy of about 100 eV (Stern *et al.*, 2009), after which it drops sharply to zero. Fig. 5 illustrates this behavior and the values shown are determined by the deconvolution results described here. Because of the presence of different atoms, the energies of the PEs vary, especially from the heavier solvent Na and Cl atoms. We approximate this by a weighted averaging over the PE energies. The form of the energy-deposition function for a PE emitted with a positive component along the X-ray polarization is expressed in the following way:

$$\begin{cases} D_{\rm PE}(x) = a\exp(\alpha|x|)\cos\left(\dfrac{\pi x}{2d}\right) & \text{for } |x| \le d \\ D_{\rm PE} = 0 & \text{for } |x| > d \end{cases}. \quad (6)$$

This function has qualitatively the correct theoretically expected form. a is the energy deposited per unit length along the X-ray polarization direction at $x = 0$ and is evaluated theoretically. For the large initial average PE energy, $E_{\rm PE}$, relative to the core binding energies of the crystal atoms the evaluation is quite reliable. Its value is given in Table 1. It also follows that

$$E_{\rm PE} = \int_0^\infty D_{\rm PE}\,{\rm d}x. \quad (7)$$

Evaluating this integral yields

$$\alpha = \frac{2a}{E_{\rm PE}}\left[\frac{\exp(\alpha d)\alpha d\pi/2 - \alpha^2 d^2}{\alpha^2 d^2 + (\pi/2)^2}\right]. \quad (8)$$

α and d can be expressed in terms of a single parameter $\beta = \alpha d$. We use β as our second fit parameter. The third fit parameter γ is the damage per deposited unit energy per unit mass. The PE energy-deposition function $D_{\rm PE}(x)$ and $\overline{B}_{\rm PE}(x)$ are proportional to each other,

$$\overline{B}_{\rm PE}(x) = \gamma\eta_{\rm PE}\frac{D_{\rm PE}(x)}{E_{\rm PE}}, \quad (9)$$

where $\eta_{\rm PE}$ is the PE fraction of the photon energy and $\overline{B}_L = \gamma\eta_{\rm L}$, where $\eta_{\rm L}$ is the fraction of the photon energy deposited locally.

Note that $\eta_{\rm PE} + \eta_{\rm L}$ is slightly larger than unity because Compton electrons excited by scattered photons are now also being included in the local damage.

The values of these three parameters were found by best fitting the experimentally observed damage $B_{\rm O}(x)$ and the corresponding calculated values as a function of the distance from the center of the incident beam. The fit results are shown in Fig. 4, the fit parameters are presented in Table 1 and the energy-deposition distribution functions are shown in Fig. 6.

We have checked the robustness of our results with respect to changes in various parameters. In particular, moving the sample along the ω axis as a result of the 3° rotation would

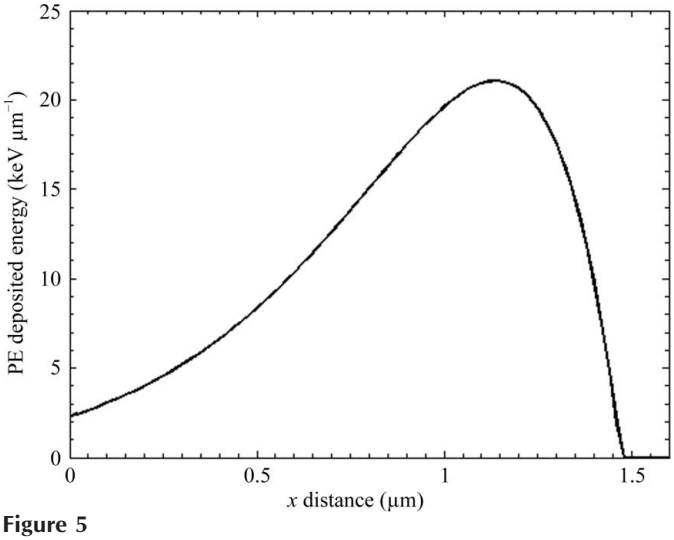

Figure 5
The deposited energy per micrometre for a weighted average PE emitted with positive component along the polarization (x direction). The penetration depth is 1.5 ± 0.2 μm.

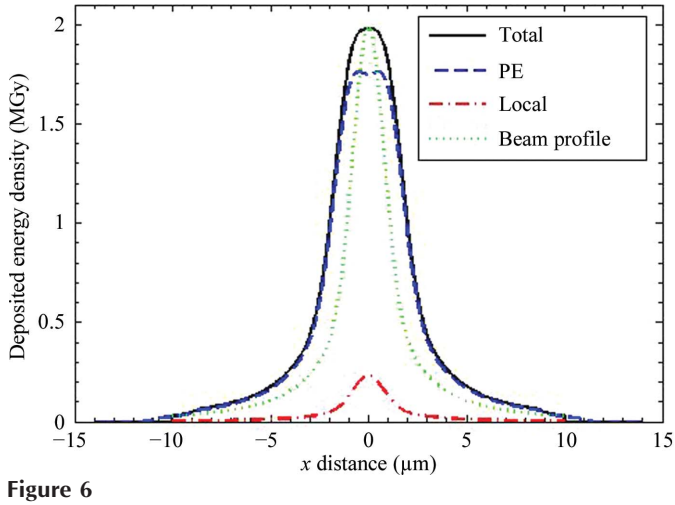

Figure 6
The distribution of energy-deposition density as a function of x distance for the total, PE and local doses. The beam profile is shown for comparison.

have the effect of broadening the probe beam. We found that broadening the probe beam by as much as 0.1 μm reduces the best fit quality significantly, indicating that the ω drive moved less than 0.1 μm along its axis. Changing the penetration depth by 0.2 μm also degraded the fit quality by a factor of 1.5.

Using the fit parameters thus obtained, calculations were made (see Fig. 5) of the energy per micrometre deposited by a single weighted average PE of 17.35 keV traveling to the right with positive x-component [*i.e.* $D_{\rm PE}(x)$] and its penetration depth from its origin. The PE deposits its energy either to the left or to the right with equal probability depending on the direction of its initial velocity. The calculation included the fact that the initial direction of the PEs has the distribution of Fig. 1. Notice that the resulting penetration depth is $d = 1.5 \pm 0.2$ μm. The distribution of Fig. 1 has an average x value of 2/3 of the PE penetration distance along its initial direction, giving an average PE penetration distance of 2.2 ± 0.3 μm. This value is significantly less than the theoretically estimated value of 4.2 μm (Nave & Hill, 2005).

Without the Lorentzian variable $\sigma_{\rm LO}^2$ the sum of the square of differences (SSD) between the best fit results and the measurements divided by the seven degrees of freedom was 0.0013, while with the variable, which reduced the degrees of freedom to six, it decreased to 0.00060, a significant improvement. Since SSD divided by degrees of freedom equals the square of the uncertainty of B (Bevington & Robinson, 2003), the uncertainty of the B factor is estimated to be ± 0.025 Å^2.

The distribution of energy-deposition density between local and PE components is shown in Fig. 6. The distribution of the energy deposited locally is proportional to the distribution of the photon flux in the beam. On the other hand, the distribution of the energy deposited by the PEs differs from that shown in Fig. 5 because it is convoluted with the spatial beam flux distribution shown in Fig. 2.

Taking into account the above results, calculations were made of the optimal conditions necessary to obtain minimal damage, shown in Fig. 7. The X-ray beams are focused down to vertical lines of Gaussian shape with root-mean-square width $\sigma_{\rm opt} = 0.20$ μm and a distance between lines of $d_{\rm opt} = 2.0$ μm, yielding a mitigation of damage equal to 2.0.

In evaluating the mitigation of radiation damage by focusing, a figure of merit is used that is defined as the ratio of the damage in the sample under uniform irradiation to the damage in the focused regions when both regions have the same diffraction signal. Since the focused regions comprise only a fraction of the sample, the X-ray exposure in them must be suitably increased over that in the uniformly irradiated region. To have a mitigation of damage greater than one, the PE damage in the focused configuration must be preferentially distributed in the spaces between focuses.

The resulting distribution of deposited energy density is shown in Fig. 8 for a single periodic unit. Note that within the focus under optimal conditions the energy deposited locally and the energy deposited by the PEs within the irradiated region are comparable. This demonstrates that the local energy deposited plays an important role in determining the optimal value of the mitigation. Note that the overwhelming majority of the PE energy is deposited in the spaces between the focuses. The local energy distribution is proportional to the focus profile and is confined to the focused irradiated region.

Finally, the third variable, the ratio between the damage B at a given point and the energy per unit mass deposited at that point for 18.6 keV photons, was found to be $\gamma = 0.75$ Å^2 MGy^{-1}. Taking into account possible uncertainties in evaluating γ, this value is somewhat but not significantly outside of the uncertainty of the value for a uniformly irradiated lysozyme crystal of 0.90 ± 0.1 Å^2 MGy^{-1} (Kmetko *et al.*, 2006).

5. Discussion

Irradiating protein crystals with a line-focus mini-beam leads to radiation damage outside the exposed region. This damage is caused by the generation of PEs and we have measured the

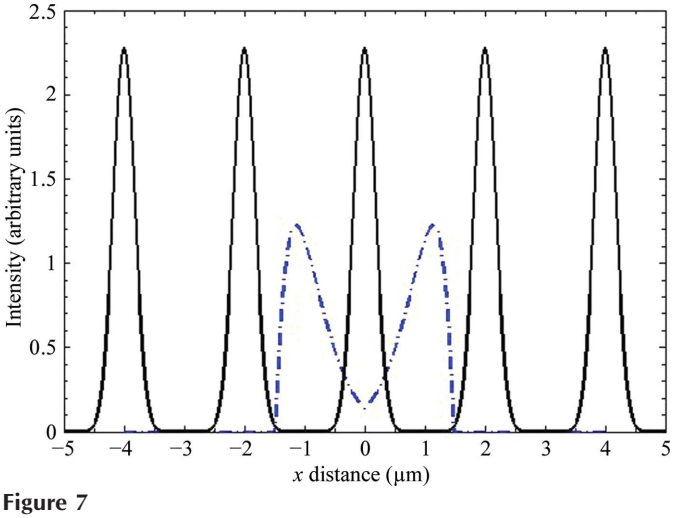

Figure 7
The optimal configuration to obtain minimal damage. The dotted/dashed line is the distribution of the PE dose and the solid lines are the vertical line-focused mini-beams.

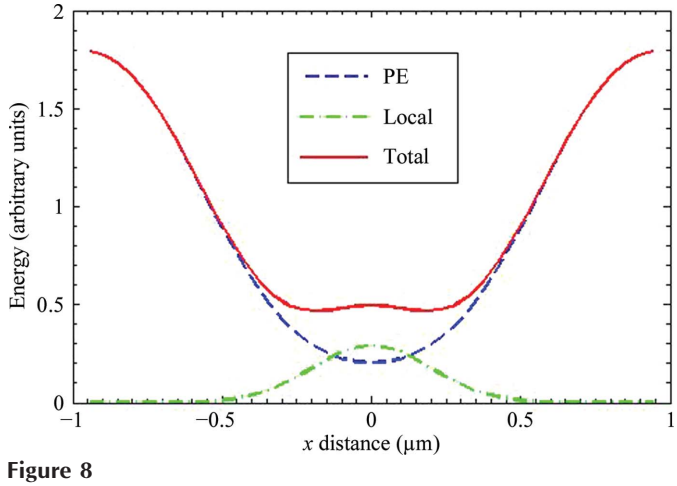

Figure 8
Relative energy deposited under optimal conditions as a function of distance. Dotted/dashed line, local; dashed line, PE; solid line, total. The local line shows the beam profile of the irradiated region.

penetration depth of PEs produced in a lysozyme crystal exposed to 18.6 keV X-rays. If a solvent (or macromolecule) adds a large number of heavier atoms (such as P, S, Cl, Br and Se) to a macromolecular crystal, the possibility of mitigating radiation damage by focusing X-rays in larger crystals is significantly degraded. Focusing does help for small crystals by concentrating the X-rays on only the crystal, eliminating unnecessary background. However, the mitigatation of the damage inside a crystal is especially degraded by the heavier atoms when focused beams are used because they increase the local damage inside the focused region. The increased damage is caused by the greater PE emission cross-section multiplied by the larger binding core-electron energy and the accompanying decrease of the PE energy, which increases its deposition of energy per unit distance within the focus. The Na and Cl atoms increased the number of emitted PEs by 35%. They also increase the average core-hole energy by 50%, causing a 50% increase in the local energy deposition. In spite of the fact that the local energy deposited is small compared with the PE energy, its effect on radiation damage is enhanced because in the optimum configuration most of the PE damage occurs outside the irradiated region, while the local damage is all concentrated within the irradiated region. Thus, relatively the deleterious effect of the local damage is amplified by focusing, as indicated in Fig. 8 compared with Fig. 6.

A universal way to mitigate radiation damage in both large and small crystals is to minimize the localized damage by using solvent atoms with as low a Z as possible in growing the crystals since localized damage increases dramatically with Z. In the example of the lysozyme crystal employed in this study each NaCl molecule inserted into the crystal from the solvent produced a dose that was enhanced by more than 82 times over that of a typical protein atom. To quantify the deleterious effect of NaCl, the calculation of the optimum configuration to minimize radiation damage was repeated without NaCl in the crystal. In this case the improvement over uniform exposure rose to 2.5 from 2.0. Also, both the mini-beam and uniform illumination cases decreased their damage further by the same factor of 1.35 owing to decreased PE production.

Decreasing the width of the focus lowers the PE damage in the irradiated region, which is a positive effect. However, it also has a negative effect because less of the sample contributes to the diffraction signal, requiring an increase of exposure and damage in the irradiated region to give the same signal as uniform illumination. The optimum condition is where these two effects change equally.

In our measurements the maximum dose was under 2.0 MGy, which is well within the region where uniform irradiation measurements (Kmetko *et al.*, 2006) find that the lysozyme damage remains linear with dose, and is also well below the Henderson limit of 20 MGy (Henderson, 1990) and the Garman limit of 30 MGy (Owen *et al.*, 2006) beyond which the data are suspect. Since the B factor varies linearly with intensity and its Debye–Waller factor varies exponentially as $\exp(-B/4r_j^2)$, then its effect varies linearly with B as $(1 - B/4r_j^2)$ only for small doses where $B/4r_j^2$ is small compared with 1, as in our case.

When the dose is an order of magnitude greater, the effect of B on the diffraction intensity is no longer linear. In this case, within the focus, where the Debye–Waller effect may vary from linear to nonlinear, the average value of B is incorrectly determined by any simple averaging of Bragg peak intensities because of the nonlinearity. With uniform illumination, where B is also uniform, this is not a problem. Fortunately, this is still true for optimal configuration focusing in spite of the intensity varying greatly within the focus because, as seen in Fig. 8 for optimal mitigation, the energy deposited, and thus B, has little variation within the illuminated region. However, for non-optimal configuration focusing, correct determination of the average of B will need to account for possible large variations within the focus, especially for point focusing.

Line focusing has many advantages over point focusing in mitigating radiation damage. A line focus more efficiently deposits the PE dose outside the irradiated region because it takes advantage of the asymmetric distribution of its dose, which is directed on average outward along the X-ray polarization. The line focus requires less X-ray exposure per unit area than a point focus to produce the same diffraction signal, causing less damage. In addition, it allows a larger volume of the crystal to be irradiated, leading to significantly stronger diffraction data. The line focus thus has less severe problems with variations of intensity in the focus. To our knowledge, there has not been any published strategy to estimate how point focuses should be distributed over a small or large crystal to have mitigation advantage over uniform irradiation as has been performed here for line focus.

6. Summary and conclusions

Measurements of the spatial dependence of radiation damage in a lysozyme crystal were made using a micrometre-sized line-focus mini-beam in order to quantify the mitigation of damage in the diffracting irradiated region by separating the much greater PE dose outside the irradiated region. In a previous publication (Stern *et al.*, 2009), the feasibility of this possibility was shown under the assumption that the irradiated region had a constant intensity and the penetration depth of 20 keV PEs was 5–6 μm. In this report, we determined a much smaller penetration depth of ∼1.5 μm for ∼17.35 keV PEs using a line-focus mini-beam whose intensity profile consists of a Gaussian shape with relatively wide tails (Fig. 2) and a deconvolution method that utilized the beam profile. The reliability of the deconvolution results was checked by varying all possible parameters and our result was found to be quite robust. The reliability of the deconvolution results is further confirmed by both the agreement of the ratio between B and dose with that determined for lysozyme under uniform irradiation and the reasonable estimate of the uncertainties in B.

Results for our lysozyme crystal were then calculated to obtain the optimum configuration shown in Fig. 7, which reduced radiation damage in the irradiated area in a large crystal, yielding mitigation of damage equal to 2.0. Unfortunately, the optimum configuration of 18.6 keV photons is technically challenging using current technology, requiring a

significant improvement of the line focus of our lenses by eliminating the long tails shown in Fig. 2 and sharpening the Gaussian root-mean-square width by a factor of 5. To alleviate this obstacle, it was suggested that the PE penetration depth should be more than doubled by using more energetic X-ray photons (>26 keV). Theory (Stern *et al.*, 2009) suggests that the penetration depth increases as $E_{\rm PE}^2$.

Alhough under uniform irradiation conditions local damage is negligible compared with that from PEs, this is changed by focusing, which enhances its effect. This is clearly demonstrated in Fig. 8 for the optimum configuration, where the local damage in a lysozyme crystal is comparable to the PE damage in the irradiated region, while in uniform illumination and in the far from optimum configuration of Fig. 6 the PE damage greatly dominates. Thus, any decrease in the local damage, such as eliminating the addition of heavier atoms in the solvent, will have a greater beneficial effect in focusing compared with uniform irradiation, as is discussed more fully in §5.

The observed shorter PE penetration depth than predicted by the present theory found by our measurements suggests to us that previous calculations underestimate the effects of scattering. Further careful measurements of the PE penetration depth as a function of PE energy will help to establish the best conditions for the optimal mitigation of damage and will help in calculating how to minimize the deteriorating effects of heavy atoms.

The authors wish to thank members of the Structural Biology Center at Argonne National Laboratory for their help with data collection on the 19-ID beamline and Dr Norma Duke for providing lysozyme crystals. A discussion with Professor Seidler of the University of Washington was most helpful. This work was supported by the National Science Foundation (NSF) under Grant No. 0650547 and by the US Department of Energy, Office of Biological and Environmental Research under contract No. DE-AC02-06CH11357. The lenses were fabricated in part at the Brookhaven National Laboratory CFN supported by the US DOE, Office of Basic Energy Sciences under Contract No. DE-AC02-98CH10886 and in part at the Cornell CNF, a member of the NNIN, supported by the NSF.

References

Alkire, R. W., Duke, N. E. C. & Rotella, F. J. (2008). *J. Appl. Cryst.* **41**, 1122–1133.

Bevington, P. R. & Robinson, D. K. (2003). *Data Reduction and Error Analysis for the Physical Sciences*, 3rd ed. Boston: WCB/McGraw–Hill.

Borek, D., Cymborowski, M., Machius, M., Minor, W. & Otwinowski, Z. (2010). *Acta Cryst.* D**66**, 426–436.

Borek, D., Ginell, S. L., Cymborowski, M., Minor, W. & Otwinowski, Z. (2007). *J. Synchrotron Rad.* **14**, 24–33.

Chinte, U., Shah, B., Chen, Y.-S., Pinkerton, A. A., Schall, C. A. & Hanson, B. L. (2007). *Acta Cryst.* D**63**, 486–492.

Cowan, J. A. & Nave, C. (2008). *J. Synchrotron Rad.* **15**, 458–462.

Evans-Lutterodt, K., Ablett, J. M., Stein, A., Kao, C. C., Tennant, D. M., Klemens, F., Taylor, A., Jacobsen, C., Gammel, P. L., Huggins, H., Ustin, S., Bogart, G. & Ocola, L. (2003). *Opt. Express*, **11**, 919–926.

Garman, E. F. & Nave, C. (2009). *J. Synchrotron Rad.* **16**, 129–132.

Garman, E. F. & McSweeney, S. M. (2007). *J. Synchrotron Rad.* **14**, 1–3.

Gonzalez, A. & Nave, C. (1994). *Acta Cryst.* D**50**, 874–877.

Hanson, B. L., Harp, J. M., Kirschbaum, K., Schall, C. A., DeWitt, K., Howard, A., Pinkerton, A. A. & Bunick, G. J. (2002). *J. Synchrotron Rad.* **9**, 375–381.

Henderson, R. (1990). *Proc. R. Soc. London B*, **241**, 6–8.

Holton, J. M. (2009). *J. Synchrotron Rad.* **16**, 133–142.

Kmetko, J., Husseini, N. S., Naides, M., Kalinin, Y. & Thorne, R. E. (2006). *Acta Cryst.* D**62**, 1030–1038.

Leung, A. K. W., Park, M. M. V. & Borhani, D. W. (1999). *J. Appl. Cryst.* **32**, 1006–1009.

Meents, A., Gutmann, S., Wagner, A. & Schulze-Briese, C. (2010). *Proc. Natl Acad. Sci. USA*, **107**, 1094–1099.

Meents, A., Wagner, A., Schneider, R., Pradervand, C., Pohl, E. & Schulze-Briese, C. (2007). *Acta Cryst.* D**63**, 302–309.

Minor, W., Cymborowski, M., Otwinowski, Z. & Chruszcz, M. (2006). *Acta Cryst.* D**62**, 859–866.

Moukhametzianov, R., Burghammer, M., Edwards, P. C., Petitdemange, S., Popov, D., Fransen, M., McMullan, G., Schertler, G. F. X. & Riekel, C. (2008). *Acta Cryst.* D**64**, 158–166.

Nave, C. & Hill, M. A. (2005). *J. Synchrotron Rad.* **12**, 299–303.

Nowak, E., Brzuszkiewicz, A., Dauter, M., Dauter, Z. & Rosenbaum, G. (2009). *Acta Cryst.* D**65**, 1004–1006.

Owen, R. L., Rudiño-Piñera, E. & Garman, E. F. (2006). *Proc. Natl Acad. Sci. USA*, **103**, 4912–4917.

Paithankar, K. S., Owen, R. L. & Garman, E. F. (2009). *J. Synchrotron Rad.* **16**, 152–162.

Petrova, T., Ginell, S., Mitschler, A., Kim, Y., Lunin, V. Y., Joachimiak, G., Cousido-Siah, A., Hazemann, I., Podjarny, A., Lazarski, K. & Joachimiak, A. (2010). *Acta Cryst.* D**66**, 1075–1091.

Petrova, T., Lunin, V. Y., Ginell, S., Hazemann, I., Lazarski, K., Mitschler, A., Podjarny, A. & Joachimiak, A. (2009). *J. Mol. Biol.* **387**, 1092–1105.

Ravelli, R. B. & Garman, E. F. (2006). *Curr. Opin. Struct. Biol.* **16**, 624–629.

Sanishvili, R., Nagarajan, V., Yoder, D., Becker, M., Xu, S., Corcoran, S., Akey, D. L., Smith, J. L. & Fischetti, R. F. (2008). *Acta Cryst.* D**64**, 425–435.

Sliz, P., Harrison, S. C. & Rosenbaum, G. (2003). *Structure*, **11**, 13–19.

Southworth-Davies, R. J., Medina, M. A., Carmichael, I. & Garman, E. F. (2007). *Structure*, **15**, 1531–1541.

Stern, E. A., Yacoby, Y., Seidler, G. T., Nagle, K. P., Prange, M. P., Sorini, A. P., Rehr, J. J. & Joachimiak, A. (2009). *Acta Cryst.* D**65**, 366–374.

Takeda, K., Kusumoto, K., Hirano, Y. & Miki, K. (2010). *J. Struct. Biol.* **169**, 135–144.